

Realization of an Acoustic Third-Order Topological Insulator

Haoran Xue,¹ Yahui Yang,¹ Guigeng Liu,¹ Fei Gao,² Yidong Chong,^{1,3,*} and Baile Zhang^{1,3,†}

¹*Division of Physics and Applied Physics, School of Physical and Mathematical Sciences, Nanyang Technological University, Singapore 637371, Singapore*

²*State Key Laboratory of Modern Optical Instrumentation, and College of Information Science and Electronic Engineering, Zhejiang University, Hangzhou 310027, China*

³*Centre for Disruptive Photonic Technologies, Nanyang Technological University, Singapore 637371, Singapore*



(Received 7 February 2019; published 21 June 2019)

The recent discovery of higher-order topological insulators (TIs) has opened new possibilities in the search for novel topological materials and metamaterials. Second-order TIs have been implemented in two-dimensional (2D) systems exhibiting topological “corner states,” as well as three-dimensional (3D) systems having one-dimensional (1D) topological “hinge states.” Third-order TIs, which have topological states three dimensions lower than the bulk (which must thus be 3D or higher), have not yet been reported. Here, we describe the realization of a third-order TI in an anisotropic diamond-lattice acoustic metamaterial. The bulk acoustic band structure has nontrivial topology characterized by quantized Wannier centers. By direct acoustic measurement, we observe corner states at two corners of a rhombohedronlike structure, as predicted by the quantized Wannier centers. This work extends topological corner states from 2D to 3D, and may find applications in novel acoustic devices.

DOI: [10.1103/PhysRevLett.122.244301](https://doi.org/10.1103/PhysRevLett.122.244301)

Higher-order TIs [1–20] are a new class of topological materials supporting a generalization of the bulk-boundary correspondence principle, in which topological states are guaranteed to exist along boundaries two or more dimensions lower than that of the bulk [1–5]. In standard TIs, topological edge states occur at one lower dimension than the bulk [21,22]; for instance, a quantum Hall insulator has a 2D bulk and topological states on 1D edges. Such 1D edge states have also been demonstrated in a few classical analogs [23,24]. By contrast, a 2D second-order TI supports zero-dimensional (0D) topological “corner states.” Such a lattice was first devised based on quantized quadrupole moments [1,2] and quickly realized in mechanical [6], electromagnetic [7], and electrical [9] metamaterials. Later, another type of 2D second-order TI based on quantized Wannier centers was proposed [25–27] and demonstrated in acoustic metamaterials [10,11]. In 3D materials, second-order TI behavior has been observed in the form of 1D topological “hinge states” in bismuth [20].

According to theoretical predictions, TIs of arbitrarily high order are possible. However, in real materials the bulk is at most 3D. Thus, barring the use of synthetic dimensions [28,29], the only remaining class of high-order TI is a *third-order* TI with 3D bulk and 0D corner states. As of this writing, no such material has been reported in the literature, although there exists a theoretical proposal based on quantized octupole moments [1,2].

Here, we realize a third-order TI in a 3D acoustic metamaterial, observing topological states at the corners of a rhombohedron-like sample. This third-order TI is based on the extension of Wannier-type second-order TIs to three dimensions [25,27], and can be regarded as a 3D generalization of the classic 1D Su-Schrieffer-Heeger (SSH) model [30]. Just as in the SSH case, the eigenmode polarizations are quantized by lattice symmetries, and the Wannier centers are pinned to high-symmetry points; the mismatch between the Wannier centers and lattice truncations gives rise to charge fractionalization and hence lower-dimensional topological boundary states [25,27]. This mechanism has previously been used to implement second-order TIs in acoustic kagome lattices [10,11].

The acoustic metamaterial is based on an anisotropic diamond lattice, with cubic unit cell shown in Fig. 1(a). The lattice constant is $a/\sqrt{2}$ and the three primitive lattice vectors are $\mathbf{a}_1 = (a/2, a/2, 0)$, $\mathbf{a}_2 = (0, a/2, a/2)$, $\mathbf{a}_3 = (a/2, 0, a/2)$, where a is the side length of the cubic cell. The two sublattice atoms are located at $(0, 0, 0)$ and $(a/4, a/4, a/4)$. There are two sets of nearest-neighbor couplings. The couplings along [111] [plotted in red in Fig. 1(a)] have strength t_2 , and those along other directions (plotted in blue) have strength t_1 . The theoretical tight-binding analysis of this lattice has been performed by Ezawa [27], who showed that when $|t_1/t_2| < 1/3$, the lattice is a higher-order TI of the Wannier type. The Wannier center is located at (P_x, P_y, P_z) , where

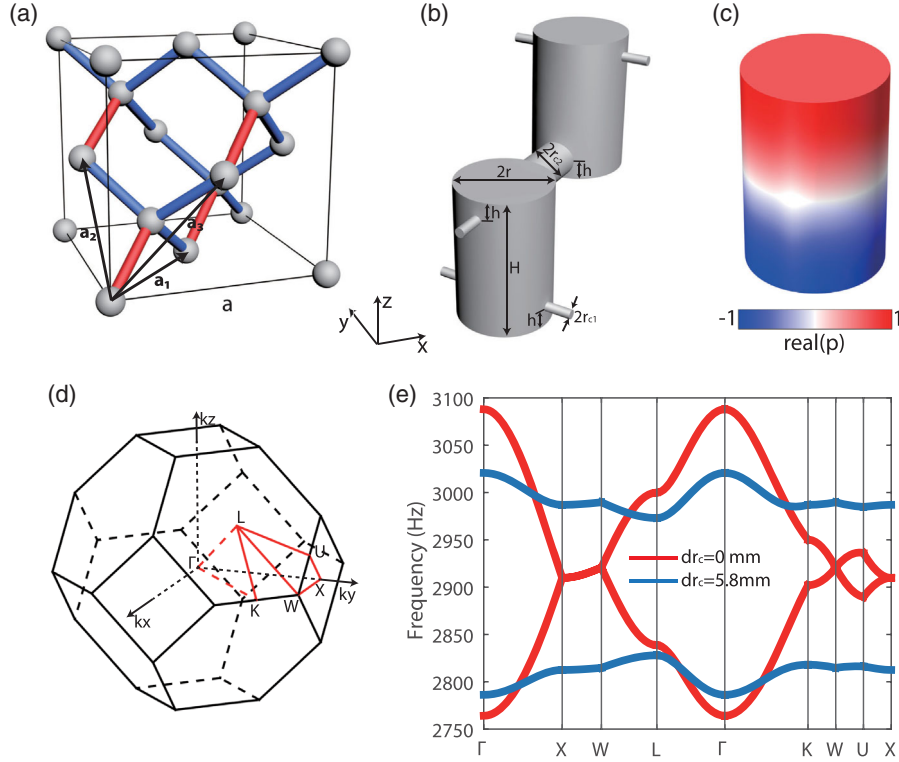


FIG. 1. Structure and bulk dispersion of acoustic anisotropic diamond lattice. (a) Schematic of the cubic cell of an anisotropic diamond lattice. Red (blue) bonds indicate couplings with strength $t_{2(1)}$. (b) The unit cell of the acoustic anisotropic diamond lattice. All parameter values are given in the main text. (c) Acoustic pressure profile for the resonator eigenmode of interest in this work. (d) The first Brillouin zone of the anisotropic diamond lattice. (e) Simulated bulk bands of acoustic anisotropic diamond lattice shown in (b). Red curves show the band structure for $dr_c = 0$ mm ($r_{c1} = r_{c2} = 4.9$ mm), and blue curves show the band structure for $dr_c = 5.8$ mm ($r_{c1} = 2$ and $r_{c2} = 7.8$ mm), where $dr_c = r_{c2} - r_{c1}$.

the polarization along each direction is given by $P_i = -(1/V) \int_{\text{BZ}} A_i d^3k$, with V being the volume of the first Brillouin zone and $A_i = -i \langle \psi | \partial_{k_i} | \psi \rangle$ being the Berry connection of the lowest band. For $|t_1/t_2| < 1/3$, the Wannier centers are fixed at $(1/2, 1/2, 1/2)$, corresponding to the centers of the red bonds in Fig. 1(a) (see Supplemental Material A [31] for tight-binding calculations). Thus, when cutting through these bonds to form a finite sample, fractional charges reside at the boundaries, similar to the SSH chain [30] and its previously studied 2D generalizations [25–27]. In the present 3D case, the same principle predicts the existence of topological states at certain corners, as well as the existence of surface states on certain 2D surfaces of the sample.

We now implement an acoustic metamaterial realization of the above tight-binding model using coupled acoustic resonators [32–36], as shown in Fig. 1(b). The two identical thick cylindrical resonators correspond to the two sublattice atoms in Fig. 1(a), connected and coupled by other thinner cylindrical waveguides. The entire structure is filled with air, and the walls are regarded as hard boundaries. The three lattice vectors are the same as in the tight-binding model of Fig. 1(a),

with $a = 175$ mm. The height (H) and radius (r) of each cylindrical resonator are 60 and 20 mm, respectively. For these parameters, a single cylindrical resonator supports the mode of interest at 2883.3 Hz, whose profile is shown in Fig. 1(c). The two sets of coupling strength are realized by tuning the radius of the connecting waveguides. The larger connecting waveguides, with radius r_{c2} , correspond to t_2 bonds in Fig. 1(a); the others, with radius r_{c1} , correspond to t_1 bonds. All connecting waveguides are located at $h = 8.125$ mm, measured from either the top or bottom of each resonator, as indicated in Fig. 1(b).

When $r_{c1} = r_{c2}$ (i.e., $t_1 = t_2$), the bulk band structure exhibits nodal lines [Fig. 1(e), red curve; see Fig. 1(d) for the 3D Brillouin zone] [27,37]. The higher-order TI phase ($|t_1/t_2| < 1/3$) is achieved by tuning the radii of the connecting waveguides. The blue curve in Fig. 1(e) shows the simulated bulk band structure for $r_{c1} = 2$ and $r_{c2} = 7.8$ mm, which has a band gap between the two bands. By fitting simulated dispersions with the tight-binding calculation, t_1/t_2 is estimated as 0.076 (see Supplemental Material A [31]), indicating that the system is in the higher-order TI phase.

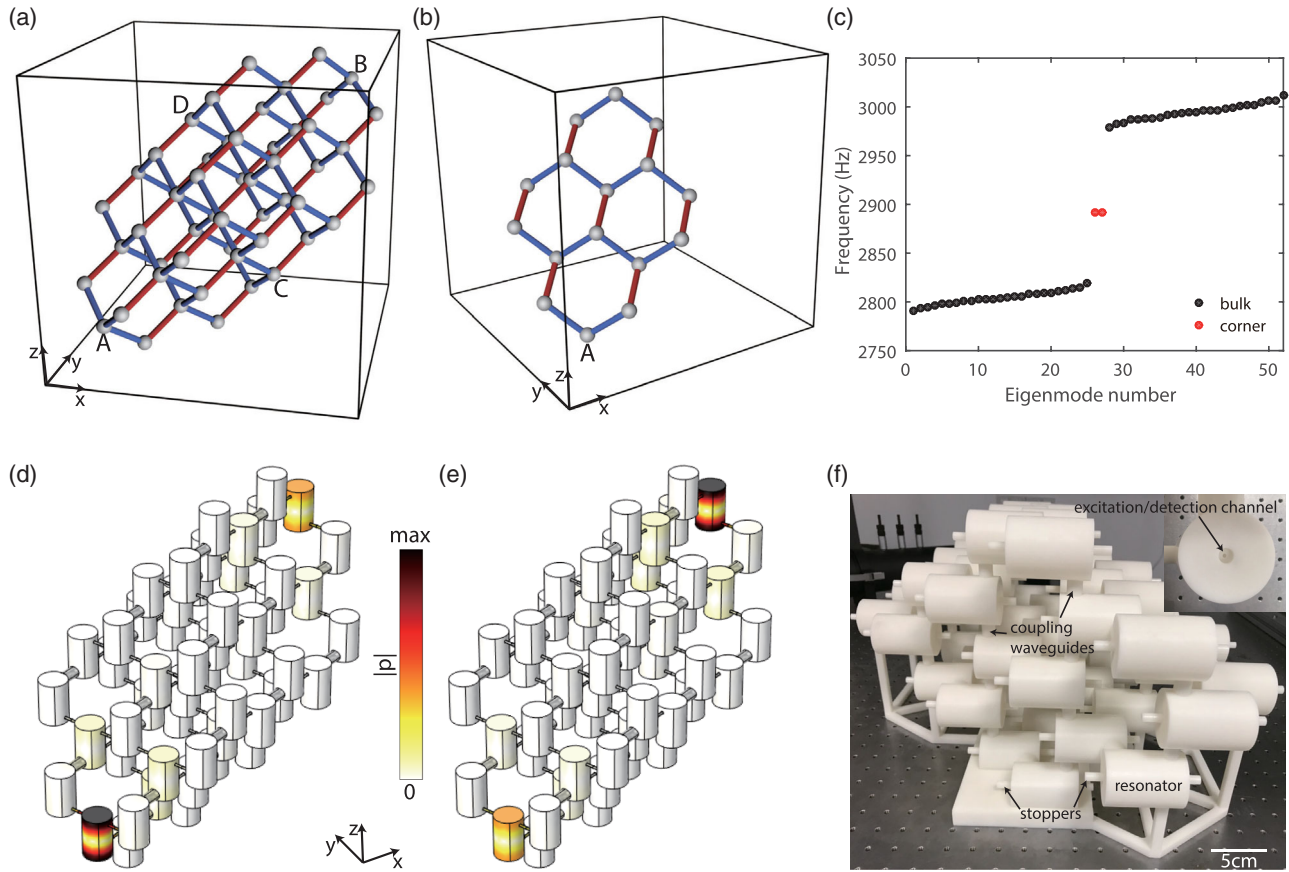


FIG. 2. Topological corner states on a rhombohedronlike sample. (a) Schematic of the rhombohedronlike structure. (b) $(\bar{1}\bar{1}1)$ surface atoms of the structure shown in (a). (c) Simulated eigenfrequencies of the finite acoustic lattice. Black and red dots represent bulk and corner states, respectively. (d),(e) Simulated eigenmode profiles of the two corner states. (f) Photograph of the fabricated rhombohedronlike sample containing 52 resonators. The inset shows an enlarged view of a resonator with one stopper removed.

A third-order TI is characterized by the existence of topological corner states at certain corners of a finite 3D sample. We consider a rhombohedronlike structure [Fig. 2(a)] containing six rhombus-shaped surfaces [see Fig. 2(b) for the $(\bar{1}\bar{1}1)$ surface]. Each surface constitutes a finite anisotropic honeycomb lattice and can be regarded as a second-order TI [27]. Corner states should occur at the two corner resonators, labeled “A” and “B” in Fig. 2(a), because all atoms are connected to red bonds (where the Wannier centers lie) except those at A and B. To check this prediction, we perform acoustic simulations on a structure containing 52 resonators, shown in Figs. 2(d)–2(e). The results, shown in Fig. 2(c), reveal two in-gap modes at around 2891 Hz, between the upper bulk band around 3000 Hz and the lower bulk band around 2800 Hz. The eigenmode patterns, plotted in Figs. 2(d)–2(e), reveal that the acoustic pressure is highly concentrated on the two corners, verifying the existence of the third-order topological boundary states.

To experimentally demonstrate this phenomenon, we fabricate a sample [see Fig. 2(f)] through stereo-lithography 3D printing, with the same parameters as in the preceding simulations. We identify the extents of the upper and lower bulk bands by measuring bulk transmission through two resonators labeled “C” and “D” in Fig. 2(a). As shown in Fig. 3(a), the spectrum exhibits two clear peaks corresponding to the upper and lower bulk bands. Next, we measure the local acoustic response at the two corner resonators, A and B (see Supplemental Material D for details [31]). For both resonators, we observe a peak at around 2900 Hz, corresponding to the corner states (see Supplemental Material B regarding the robustness of these corner states [31]). From the measured spectra shown in Fig. 3(b), the quality factor of the corner states is around 60, similar to the quality factor for an isolated resonator. The main loss channels are material absorption and leakage from the small holes used for excitation and detection (see Supplemental Material E [31]). Finally, we repeat the acoustic response measurement for all resonators,

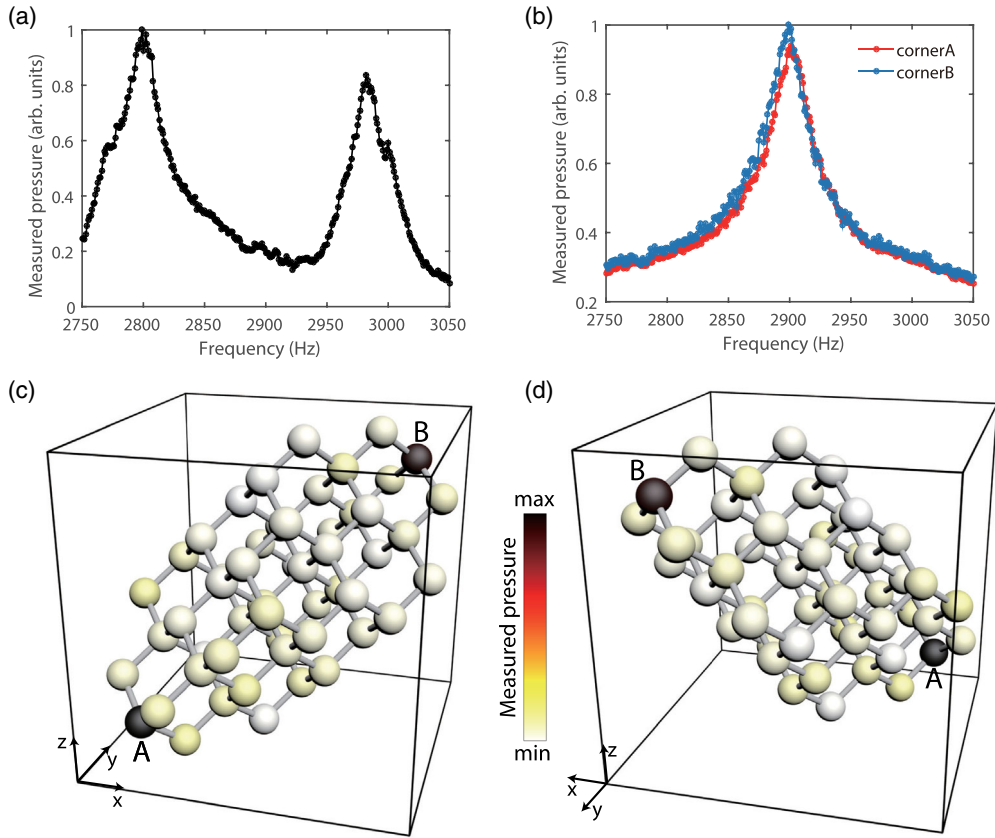


FIG. 3. Experimental observation of corner states in a rhombohedron-like acoustic structure. (a) Measured bulk transmission spectrum. (b) Measured spectra at the two corner sites indicated in (c) and (d). (c),(d) Measured pressure maps at 2900 Hz, viewed from the front (c) and back (d). The illustration of the structure is simplified for clarity; for the real structure see Figs. 2(d)–2(f). The balls correspond to the cylindrical resonators and the gray bonds indicate the couplings. The color of each ball represents the measured acoustic pressure at that site, as measured at the top of the cylindrical resonator. The color map does not apply to the bonds.

constructing an intensity map of the lattice equivalent to the local density of states. The results of these measurements, conducted at the peak frequency of the corner resonances (2900 Hz), are plotted in Figs. 3(c)–3(d) from different view angles. The acoustic pressure is indeed highly concentrated at the two relevant corners, with negligible response at the bulk sites, along the 2D surfaces or 1D corners, or at sample corners not corresponding to divided Wannier centers.

It is important to note that no 2D or 1D surface states are observed in this sample because the lattice is truncated in such a manner that *only* the two corner resonators are “peeled off” from the red bonds [see Fig. 2(a)]. However, it is also possible to truncate the lattice in other ways that should generate topological surface states, according to the analysis of quantized Wannier centers. Previously, it has been predicted that such surface states should exist on a (111) surface [37] (see Supplemental Material C [31]); moreover, there should be no surface states along other surfaces where the lattice truncation occurs along blue bonds. To test this prediction, we fabricated a tetrahedronlike

sample containing four different surfaces, oriented at (111), $(\bar{1}\bar{1}\bar{1})$, $(\bar{1}\bar{1}1)$, and $(1\bar{1}\bar{1})$, as shown in Fig. 4(a). We excite and measure the acoustic response at a surface resonator on the (111) surface, indicated by the red star in Fig. 4(a), and repeat the procedure for the other three surfaces. The results, plotted in Fig. 4(b), agree well with the theoretical predictions. Only along the (111) surface is there a sharp response peak, at around 2910 Hz, corresponding to the surface state. Along the other three surfaces, we observe only the two peaks corresponding to the bulk states. By performing the measurement in all the lattice resonators, we derive the map shown in Figs. 4(c)–4(d): at 2900 Hz, the response is much higher along the (111) surface than elsewhere in the lattice.

In conclusion, we have implemented a third-order TI on an acoustic anisotropic diamond lattice. Corner states and surface states were observed in a rhombohedronlike sample and a tetrahedronlike sample, respectively, in accordance with a theoretical analysis based on quantized Wannier centers. Unlike electronic systems, the absence of a Fermi level in acoustic structures makes the entire spectrum easily

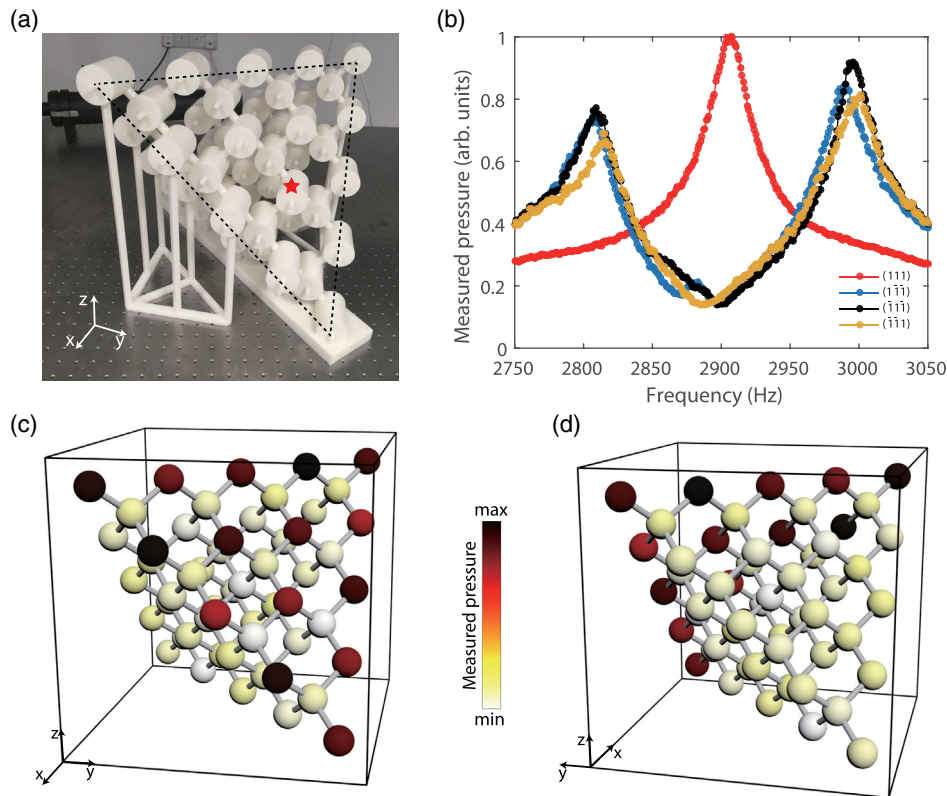


FIG. 4. Experimental demonstration of surface states on a tetrahedronlike acoustic structure. (a) Photograph of the fabricated sample. Black dashed line denotes the (111) surface. (b) Measured spectra at four surface resonators on four surfaces of the sample. The source and probe are located at the same resonator for each curve. (c),(d) Measured pressure maps at 2900 Hz, viewed from the front (c) and back (d).

accessible, allowing us to probe bulk, surface, and corner states at different frequencies. The extension of topological corner states from 2D to 3D may have potential use in applications such as acoustic manipulation and sensing [38]. We also envision that our study will inspire more experimental studies into the implementation of higher-order TIs and high-order topological semimetals [25,39,40] in higher dimensions.

The authors thank Wenzheng Ye from Zhejiang University for help on sample fabrication. This work was sponsored by Singapore Ministry of Education under Grants No. MOE2018-T2-1-022 (S), No. MOE2015-T2-2-008, No. MOE2016-T3-1-006 and Tier 1 RG174/16 (S), and National Natural Science Foundation of China under Grant No. 61801426.

*yidong@ntu.edu.sg

[†]blzhang@ntu.edu.sg

- [1] W. A. Benalcazar, B. A. Bernevig, and T. L. Hughes, Quantized electric multipole insulators, *Science* **357**, 61 (2017).
 [2] W. A. Benalcazar, B. A. Bernevig, and T. L. Hughes, Electric multipole moments, topological multipole moment

- pumping, and chiral hinge states in crystalline insulators, *Phys. Rev. B* **96**, 245115 (2017).
 [3] F. Schindler, A. M. Cook, M. G. Vergniory, Z. Wang, S. S. P. Parkin, B. A. Bernevig, and T. Neupert, Higher-order topological insulators, *Sci. Adv.* **4**, eaat0346 (2018).
 [4] J. Langbehn, Y. Peng, L. Trifunovic, F. von Oppen, and P. W. Brouwer, Reflection-Symmetric Second-Order Topological Insulators and Superconductors, *Phys. Rev. Lett.* **119**, 246401 (2017).
 [5] Z. Song, Z. Fang, and C. Fang, (d-2)-Dimensional Edge States of Rotation Symmetry Protected Topological States, *Phys. Rev. Lett.* **119**, 246402 (2017).
 [6] M. Serra-Garcia, V. Peri, R. Süsstrunk, O. R. Bilal, T. Larsen, L. G. Villanueva, and S. D. Huber, Observation of a phononic quadrupole topological insulator, *Nature (London)* **555**, 342 (2018).
 [7] C. W. Peterson, W. A. Benalcazar, T. L. Hughes, and G. Bahl, A quantized microwave quadrupole insulator with topologically protected corner states, *Nature (London)* **555**, 346 (2018).
 [8] J. Noh, W. A. Benalcazar, S. Huang, M. J. Collins, K. P. Chen, T. L. Hughes, and M. C. Rechtsman, Topological protection of photonic mid-gap defect modes, *Nat. Photonics* **12**, 408 (2018).
 [9] S. Imhof *et al.*, Topoelectrical-circuit realization of topological corner modes, *Nat. Phys.* **14**, 925 (2018).

- [10] H. Xue, Y. Yang, F. Gao, Y. Chong, and B. Zhang, Acoustic higher-order topological insulator on a kagome lattice, *Nat. Mater.* **18**, 108 (2019).
- [11] X. Ni, M. Weiner, A. Alù, and A. B. Khanikaev, Observation of higher-order topological acoustic states protected by generalized chiral symmetry, *Nat. Mater.* **18**, 113 (2019).
- [12] X. Zhang, H.-X. Wang, Z.-K. Lin, Y. Tian, B. Xie, M.-H. Lu, Y.-F. Chen, and J.-H. Jiang, Second-order topology and multidimensional topological transitions in sonic crystals, *Nat. Phys.* **15**, 582 (2019).
- [13] X. Zhang, Z.-K. Lin, H.-X. Wang, Y. Tian, M.-H. Lu, Y.-F. Chen, and J.-H. Jiang, Acoustic hierarchical topological insulators, [arXiv:1811.05514](https://arxiv.org/abs/1811.05514).
- [14] B.-Y. Xie, G.-X. Su, H.-F. Wang, H. Su, X.-P. Shen, P. Zhang, M.-H. Lu, Z.-L. Wang, and Y.-F. Chen, Visualization of higher-order topological insulating phases in two-dimensional dielectric photonic crystals, [arXiv:1812.06263](https://arxiv.org/abs/1812.06263).
- [15] X.-D. Chen, W.-M. Deng, F.-L. Shi, F.-L. Zhao, M. Chen, and J.-W. Dong, Direct observation of corner states in second-order topological photonic crystal slabs, [arXiv:1812.08326](https://arxiv.org/abs/1812.08326).
- [16] A. E. Hassan, F. K. Kunst, A. Moritz, G. Andler, E. J. Bergholtz, and M. Bourennane, Corner states of light in photonic waveguides, [arXiv:1812.08185](https://arxiv.org/abs/1812.08185).
- [17] S. Mittal, V. V. Orre, G. Zhu, M. A. Gorlach, A. Poddubny, and M. Hafezi, Photonic quadrupole topological phases, [arXiv:1812.09304](https://arxiv.org/abs/1812.09304).
- [18] Y. Ota, F. Liu, R. Katsumi, K. Watanabe, K. Wakabayashi, Y. Arakawa, and S. Iwamoto, Photonic crystal nanocavity based on a topological corner state, *Optica* **6**, 786 (2019).
- [19] M. Serra-Garcia, R. Süsstrunk, and S. D. Huber, Observation of quadrupole transitions and edge mode topology in an LC circuit network, *Phys. Rev. B* **99**, 020304(R) (2019).
- [20] F. Schindler *et al.*, Higher-order topology in bismuth, *Nat. Phys.* **14**, 918 (2018).
- [21] M. Z. Hasan and C. L. Kane, Colloquium: Topological insulators, *Rev. Mod. Phys.* **82**, 3045 (2010).
- [22] X.-L. Qi and S.-C. Zhang, Topological insulators and superconductors, *Rev. Mod. Phys.* **83**, 1057 (2011).
- [23] Z. Wang, Y. Chong, J. D. Joannopoulos, and M. Soljačić, Observation of unidirectional backscattering-immune topological electromagnetic states, *Nature (London)* **461**, 772 (2009).
- [24] Y. Ding, Y. Peng, Y. Zhu, X. Fan, J. Yang, B. Liang, X. Zhu, X. Wan, and J. Cheng, Experimental Demonstration of Acoustic Chern Insulators, *Phys. Rev. Lett.* **122**, 014302 (2019).
- [25] M. Ezawa, Higher-Order Topological Insulators and Semimetals on the Breathing Kagome and Pyrochlore Lattices, *Phys. Rev. Lett.* **120**, 026801 (2018).
- [26] F. K. Kunst, G. Miert, and E. J. Bergholtz, Lattice models with exactly solvable topological hinge and corner states, *Phys. Rev. B* **97**, 241405(R) (2018).
- [27] M. Ezawa, Minimal models for Wannier-type higher-order topological insulators and phosphorene, *Phys. Rev. B* **98**, 045125 (2018).
- [28] M. Lohse, C. Schweizer, H. M. Price, O. Zilberberg, and I. Bloch, Exploring 4D quantum Hall physics with a 2D topological charge pump, *Nature (London)* **553**, 55 (2018).
- [29] O. Zilberberg, S. Huang, J. Guglielmon, M. Wang, K. P. Chen, Y. E. Kraus, and M. C. Rechtsman, Photonic topological boundary pumping as a probe of 4D quantum Hall physics, *Nature (London)* **553**, 59 (2018).
- [30] W. P. Su, J. R. Schrieffer, and A. J. Heeger, Solitons in Polyacetylene, *Phys. Rev. Lett.* **42**, 1698 (1979).
- [31] See Supplemental Material at <http://link.aps.org/supplemental/10.1103/PhysRevLett.122.244301> for additional tight-binding calculations, numerical simulations and experimental results.
- [32] M. Xiao, W.-J. Chen, W.-Y. He, and C. T. Chan, Synthetic gauge flux and Weyl points in acoustic systems, *Nat. Phys.* **11**, 920 (2015).
- [33] Z. Yang and B. Zhang, Acoustic Type-II Weyl Nodes from Stacking Dimerized Chains, *Phys. Rev. Lett.* **117**, 224301 (2016).
- [34] Z. Yang, F. Gao, Y. Yang, and B. Zhang, Strain-Induced Gauge Field and Landau Levels in Acoustic Structures, *Phys. Rev. Lett.* **118**, 194301 (2017).
- [35] F. Li, X. Huang, J. Lu, J. Ma, and Z. Liu, Weyl points and Fermi arcs in a chiral phononic crystal, *Nat. Phys.* **14**, 30 (2018).
- [36] C. He *et al.*, Three-dimensional topological acoustic crystals with pseudospin-valley coupled saddle surface states, *Nat. Commun.* **9**, 4555 (2018).
- [37] R. Takahashi and S. Murakami, Completely flat bands and fully localized states on surfaces of anisotropic diamond-lattice models, *Phys. Rev. B* **88**, 235303 (2013).
- [38] F. Zangeneh-Nejad and R. Fleury, Topological Fano Resonances, *Phys. Rev. Lett.* **122**, 014301 (2019).
- [39] M. Lin and T. L. Hughes, Topological quadrupolar semimetals, *Phys. Rev. B* **98**, 241103(R) (2018).
- [40] D. Călugăru, V. Juričić, and B. Roy, Higher-order topological phases: A general principle of construction, *Phys. Rev. B* **99**, 041301(R) (2019).